Acta Geotechnica (2018) 13:1027–1040
https://doi.org/10.1007/s11440-018-0700-3

RESEARCH PAPER

Continuum hydrodynamics of dry granular flows employing multiplicative elastoplasticity

Alomir H. Fávero Neto[1,2] · Ronaldo I. Borja[1]

Received: 2 March 2018 / Accepted: 6 July 2018 / Published online: 1 August 2018

Abstract

We present a Lagrangian formulation for simulating the continuum hydrodynamics of dry granular flows based on multiplicative elastoplasticity theory for finite deformation calculations. The formulation is implemented within the smoothed particle hydrodynamics (SPH) method along with a variant of the usual dynamic boundary condition. Three benchmark simulations on dry sands are presented to validate the model: (a) a set of plane strain collapse tests, (b) a set of 3D collapse tests, and (c) a plane strain simulation of the impact force generated by granular flow on a rigid wall. Comparison with experimental results suggests that the formulation is sufficiently robust and accurate to model the continuum hydrodynamics of dry granular flows in a laboratory setting. Results of the simulations suggest the potential of the formulation for modeling more complex, field-scale scenarios characterized by more elaborate geometry and multi-physical processes. To the authors' knowledge, this is the first time the multiplicative plasticity approach has been applied to granular flows in the context of the SPH method.

Keywords Debris flow · Granular flow · Landslide · Multiplicative plasticity · Smoothed particle hydrodynamics

1 Introduction

The recent events in Santa Barbara County, California [48], are a reminder of the serious threat mudslides and debris flows pose to property and human life. They also raise the question as to why predicting or mitigating landslides and debris flows remains elusive. Numerous models for landslide triggering have emerged in recent years. A majority of these models define the problem domain using grids and meshes that maintain element connectivity [3, 6–8, 14, 25, 28, 33]. However, whereas this class of models may be adequate for simulating slope responses prior to landslide triggering, they are not suitable for quantitative simulation of the very large deformation that develops after landslide initiation, which could lead to loss in element connectivity. Mesh-based numerical modeling usually breaks down due to severe element distortion when applied to phenomena such as granular flow, debris flow, and mudslides.

There has been significant progress in recent years on the numerical modeling of granular flows, debris flows, and mudslides. Apart from the traditional discrete element methods [13, 15, 47], numerous continuum methods that do not rely on any mesh or grid have emerged in the literature. Among these so-called continuum particle methods are the material point method [2, 19, 45], reproducing kernel particle method [17, 43], peridynamics [26], and smoothed particle hydrodynamics (SPH) [20, 21, 32, 37]. In general, these methods can accommodate very large deformation, and they do not suffer from severe mesh distortion since there is no mesh to deal with in the first place. Furthermore, unlike the discrete element method that requires brute-force calculations, continuum particle methods define "particles" in a continuum sense, thus significantly reducing the size of the problem to solve.

With few exceptions, a majority of meshless methods employ an Eulerian formulation to impose the equation of motion and perform the kinematical updates. While this framework may be appropriate for fluids and fluidized

✉ Ronaldo I. Borja
borja@stanford.edu

[1] Department of Civil and Environmental Engineering, Stanford University, Stanford, CA 94305, USA

[2] CNPq Scholar, Institute for Technological Research, São Paulo, SP, Brazil

media, it may not be ideal for solids and solidified materials where some memory of the loading history must be preserved, such as elastoplastic [5] and elasto-viscoplastic [42] materials. This is due to the convected term in the Eulerian formulation that results in a more complicated constitutive update. For this latter class of materials, a Lagrangian formulation is more appropriate because the description follows the material motion, thus preserving the history of loading naturally. This is especially true for the problem of landslide initiation and evolution where the sediment may fluidize from an initially solid state, subsequently flow, and later come to rest in a solidified state.

In this work, we focus specifically on the SPH framework for capturing granular flow. There have been some works in the literature on the application of SPH to investigate the stability of homogeneous slopes using modern plasticity theory [11, 12]. Benchmark simulations have also been reported in the literature to show the suitability of this approach for slope stability problems [16, 36], as well as for soil–fluid interaction problems [9, 10, 52]. More recently, a hypoplastic constitutive model has been incorporated into the SPH framework [23, 38], which was further extended to account for granular inertial effects [39]. Similar developments have been reported in [24, 46]. Common to all of these works is the lack of a unique definition of an objective stress rate for finite deformation calculations, with a majority of the works often attributing objectivity to Jaumann [41]. The use of an Eulerian kernel also comes with numerical issues such as tensile instability [22].

This paper takes a different point of view and adopts a Lagrangian finite deformation formulation for investigating the problem of granular flow with the SPH approach. The constitutive model is based on hyperelasto-plasticity that employs a multiplicative split of the deformation gradient tensor. There are numerous advantages of such an approach. First, it bypasses the issue of having to write the elastic constitutive equation in rate form, thus circumventing the question of what objective stress rate to use [42]. Second, tensile instability is avoided with the total Lagrangian approach. On top of these, since the accuracy and stability of the SPH approach are directly related to the particles' arrangement, the updated or total Lagrangian approach improves these characteristics of the method, since they rely on a more ordered configuration of particles. The use of hyperelasticity along with the multiplicative plasticity enables the state of stress to be uniquely determined from the current state of elastic strain, which depends only on the update of the particles positions, thus reducing the integration error associated with an additional integration of the elastic strain and stress rate equations. Finally, all the canonical constitutive update algorithms for infinitesimal deformation may be employed for finite deformation calculations in a form that is essentially unchanged [41].

To demonstrate the predictive capability of the proposed approach, we simulate three laboratory experiments involving granular flow. The first two simulations involve dry sand column collapse in plane strain and 3D. The numerical results are compared with the experimental results reported in [30, 31], as well as with the results of the simulations conducted by other authors. The third and final problem demonstrates the ability of the model to capture the impact force produced by granular flow on a rigid wall. For these latter simulations, we use the laboratory-scale tests on dry sand released on an inclined flume conducted by Moriguchi et al. [34] to investigate the capability of the approach to predict the impact force generated by sand on a rigid wall located at the bottom of the flume.

As for the order of presentation, Sect. 2 presents the theoretical background relevant to the multiplicative elastoplasticity theory employed in this work. Section 3 describes how the theory is incorporated into the SPH approach. Section 4 presents the numerical simulations and comparison with experimental data. Finally, Sect. 5 concludes the paper and outlines some ideas for future work.

2 Kinematics and constitutive framework

Consider a material point X interpreted to be a volume representation of an assembly of soil particles contained in a representative elementary volume with an associated reference position $\boldsymbol{X}$. We assume that this material point has moved and is now at the current configuration $\boldsymbol{x}(X) = \boldsymbol{X} + \boldsymbol{u}(X)$, where $\boldsymbol{u}(X)$ is the displacement of the material point relative to the reference configuration. The deformation gradient is given by

$$\boldsymbol{F} = \frac{\partial \boldsymbol{x}}{\partial \boldsymbol{X}} = \boldsymbol{1} + \frac{\partial \boldsymbol{u}}{\partial \boldsymbol{X}}, \tag{1}$$

where $\boldsymbol{1}$ is the second-rank identity tensor. Following Lee's theory [27], we assume a multiplicative decomposition of $\boldsymbol{F}$ into an elastic part $\boldsymbol{F}^{\mathrm{e}}$ and a plastic part $\boldsymbol{F}^{\mathrm{p}}$,

$$\boldsymbol{F} = \boldsymbol{F}^{\mathrm{e}} \cdot \boldsymbol{F}^{\mathrm{p}}. \tag{2}$$

The decomposition assumes that there exists an intermediate configuration $\boldsymbol{\chi}$ to which the material point will unload when the stresses are removed.

From these deformation gradient tensors, the elastic (left) and plastic (right) deformation tensors can be obtained from the expressions

$$\boldsymbol{b}^{\mathrm{e}} = \boldsymbol{F}^{\mathrm{e}} \cdot \boldsymbol{F}^{\mathrm{e}\mathsf{T}}, \quad \boldsymbol{C}^{\mathrm{p}} = \boldsymbol{F}^{\mathrm{p}\mathsf{T}} \cdot \boldsymbol{F}^{\mathrm{p}}. \tag{3}$$

The elastic left Cauchy–Green deformation tensor $\boldsymbol{b}^{\mathrm{e}}$ is used to determine the stresses via a hyperelastic equation of the form

$$\boldsymbol{\tau} := J\boldsymbol{\sigma} = 2\frac{\partial \Psi}{\partial \boldsymbol{b}^{\mathrm{e}}} \cdot \boldsymbol{b}^{\mathrm{e}}, \tag{4}$$

where $J = \det(\boldsymbol{F}), \boldsymbol{\sigma}$ is the Cauchy stress tensor, $\boldsymbol{\tau}$ is the Kirchhoff stress tensor, and $\Psi = \Psi(\boldsymbol{b}^{\mathrm{e}})$ is the elastic stored energy function. In expressing the stored energy function in terms of $\boldsymbol{b}^{\mathrm{e}}$, it is assumed that the material is elastically isotropic. Frame invariance then suggests that the stored energy function depends only on the principal values of $\boldsymbol{b}^{\mathrm{e}}$, i.e.,

$$\Psi = \Psi(\lambda_1^{\mathrm{e}}, \lambda_2^{\mathrm{e}}, \lambda_3^{\mathrm{e}}), \tag{5}$$

where $\lambda_A^{\mathrm{e}}, A = 1, 2, 3$, are the principal values, also called the elastic principal stretches. Since functions of invariants are also invariant, we can also write

$$\Psi = \Psi(\varepsilon_1^{\mathrm{e}}, \varepsilon_2^{\mathrm{e}}, \varepsilon_3^{\mathrm{e}}), \tag{6}$$

where $\varepsilon_A^{\mathrm{e}} = \log(\lambda_A^{\mathrm{e}}), A = 1, 2, 3$ are called the elastic logarithmic principal stretches. Spectral decomposition for isotropic elastoplasticity leads to an elastic constitutive equation of the form

$$\tau_A = \frac{\partial \Psi}{\partial \varepsilon_A^{\mathrm{e}}}, \tag{7}$$

where $\tau_A, A = 1, 2, 3$, are the principal values of $\boldsymbol{\tau}$.

To accommodate the inelastic component of deformation, we consider a rate-independent elastoplastic response in which the plastic response is contingent on the satisfaction of the yield condition

$$\mathcal{F} = \mathcal{F}(\tau_1, \tau_2, \tau_3, \kappa) = 0, \tag{8}$$

where $\mathcal{F}$ is the yield function and κ is a plastic internal variable that determines the size of the elastic region. In the preceding equation, it was assumed that $\mathcal{F}$ is an isotropic function of the Kirchhoff stress, and so only the principal values of the stress tensor are considered. The flow rule can either be associative or non-associative. For non-associative plastic flow, a plastic potential function $\mathcal{Q} \neq \mathcal{F}$ is needed, from which the flow rule can be written as

$$-\frac{1}{2}\mathcal{L}_v \boldsymbol{b}^{\mathrm{e}} = \dot{\gamma}\frac{\partial \mathcal{Q}}{\partial \boldsymbol{\tau}} \cdot \boldsymbol{b}^{\mathrm{e}}, \tag{9}$$

where $\mathcal{L}_v \boldsymbol{b}^{\mathrm{e}}$ is the Lie derivative of $\boldsymbol{b}^{\mathrm{e}}$.

The integration algorithm for the constitutive model follows the standard elastic predictor–plastic corrector scheme. In the elastic predictor phase, plastic deformation is frozen at the current state of stress, while in the plastic corrector phase the stresses are relaxed to enable the satisfaction of the yield condition. Let $\boldsymbol{b}_n^{\mathrm{e}}$ denote the current value of $\boldsymbol{b}^{\mathrm{e}}$ at time t_n. Over the time interval $[t_n, t_{n+1}]$ the relative deformation gradient is given by

$$\boldsymbol{f}_{n+1} = \frac{\partial \boldsymbol{x}_{n+1}}{\partial \boldsymbol{x}_n} = \frac{\partial \boldsymbol{x}_{n+1}}{\partial \boldsymbol{X}} \cdot \frac{\partial \boldsymbol{X}}{\partial \boldsymbol{x}_n} = \boldsymbol{F}_{n+1} \cdot \boldsymbol{F}_n^{-1}. \tag{10}$$

By freezing plastic flow during this time interval, we obtain the elastic predictor

$$\boldsymbol{b}_{n+1}^{\mathrm{e\,tr}} = \boldsymbol{f}_{n+1} \cdot \boldsymbol{b}_n^{\mathrm{e}} \cdot \boldsymbol{f}_{n+1}^{\mathsf{T}}. \tag{11}$$

From this predictor value of $\boldsymbol{b}^{\mathrm{e}}$, we can calculate the trial elastic Kirchhoff stress using the hyperelastic constitutive equation

$$\boldsymbol{\tau}_{n+1}^{\mathrm{tr}} = 2\frac{\partial \Psi}{\partial \boldsymbol{b}_{n+1}^{\mathrm{e\,tr}}} \cdot \boldsymbol{b}_{n+1}^{\mathrm{e\,tr}}. \tag{12}$$

Checking for yielding, the trial elastic predictor values are accepted if the condition $\mathcal{F}(\boldsymbol{\tau}_{n+1}^{\mathrm{tr}}, \kappa_n) \leq 0$ is satisfied; otherwise, plastic correction is performed by updating $\boldsymbol{\tau}$ and κ to enforce the yield condition $\mathcal{F}(\boldsymbol{\tau}_{n+1}, \kappa_{n+1}) = 0$.

Employing the first-order accurate backward integration scheme on the flow Eq. (9) yields

$$\boldsymbol{b}_{n+1}^{\mathrm{e}} = \exp\left(-2\Delta\gamma_{n+1}\frac{\partial \mathcal{Q}}{\partial \boldsymbol{\tau}_{n+1}}\right) \cdot \boldsymbol{b}_{n+1}^{\mathrm{e\,tr}}, \tag{13}$$

where $\Delta\gamma_{n+1}$ is the incremental plastic multiplier. After recognizing the co-axiality of $\boldsymbol{\tau}, \boldsymbol{b}^{\mathrm{e}}$ and $\boldsymbol{b}^{\mathrm{e\,tr}}$, spectral decomposition of (13) leaves the scalar equations

$$(\lambda_A^{\mathrm{e}})_{n+1}^2 = \exp\left(-2\Delta\gamma_{n+1}\frac{\partial \mathcal{Q}}{\partial \tau_{A,n+1}}\right)(\lambda_A^{\mathrm{e\,tr}})_{n+1}^2 \tag{14}$$

for $A = 1, 2, 3$. Taking the natural logarithm of both sides of the above equation results in an additive decomposition of the principal elastic logarithmic stretches of the form resembling the one obtained from the infinitesimal formulation,

$$\varepsilon_{A,n+1}^{\mathrm{e}} = \varepsilon_{A,n+1}^{\mathrm{e\,tr}} - \Delta\gamma_{n+1}\frac{\partial \mathcal{Q}}{\partial \tau_{A,n+1}}. \tag{15}$$

Together with the update equation for the plastic internal variable κ of the form

$$\kappa_{n+1} = f(\kappa_n, \Delta\gamma), \tag{16}$$

the rate-independent elastoplastic limit can be determined sequentially at each time step.

Stress-point integration consists of solving update Eq. (15) along with yield condition (8) imposed at time t_{n+1}. One can choose either the three elastic logarithmic principal stretches or the three principal values of the Kirchhoff stress tensor as the unknowns, along with the discrete consistency parameter $\Delta\gamma_{n+1}$, for a total of four unknowns. These unknowns are typically solved by a local

Newton–Raphson iteration [5, 42]. In the context of the SPH method, stress-point calculations are done locally for each particle whose motion is tracked using either a total Lagrangian or an updated Lagrangian description. The next section describes how the multiplicative plasticity framework is integrated into the SPH method to solve granular flow problems.

3 SPH implementation

The stress-point integration algorithm described in the preceding section is driven by the incremental displacement $\Delta \boldsymbol{u} = \boldsymbol{u}_{n+1} - \boldsymbol{u}_n$ of each particle, which in turn is calculated from the dynamic equation of equilibrium. Formally, the strong form of the boundary-value problem goes as follows. Consider a domain $\mathcal{B}$ bounded by surface $\partial\mathcal{B}$ in the reference configuration. Conservation of linear momentum in this domain, along with relevant boundary conditions, yields the strong form of the boundary-value problem,

$$\frac{1}{\rho_0}\mathrm{DIV}(\boldsymbol{P}) + \boldsymbol{g} = \boldsymbol{a} \quad \text{in } \mathcal{B} \times t \tag{17}$$

$$\boldsymbol{v} = \bar{\boldsymbol{v}} \quad \text{on } \partial\mathcal{B}_v \times t \tag{18}$$

$$\boldsymbol{P} \cdot \boldsymbol{N} = \boldsymbol{t}_0 \quad \text{on } \partial\mathcal{B}_t \times t \tag{19}$$

subject to initial conditions $\boldsymbol{u}, \boldsymbol{v}$, and $\boldsymbol{a}$ = given at $t = 0$. Here, $\boldsymbol{P}$ is the first Piola–Kirchhoff stress tensor, DIV is the Lagrangian divergence operator, ρ_0 is the pullback mass density in the reference configuration, $\boldsymbol{g}$ is the gravity acceleration vector, $\boldsymbol{u}, \boldsymbol{v}$, and $\boldsymbol{a}$ are the particle displacement, velocity, and acceleration, respectively, and t is time. We then solve this problem with the SPH approach. For relevant background about this approach, the reader is referred to [21, 29, 32, 49–51] and references therein.

We adopt an updated Lagrangian point of view (see [4, 51], e.g.), in which the reference configuration is the configuration at time t_n and the next configuration is at time t_{n+1} (Fig. 1). This implies that the relative deformation gradient $\boldsymbol{f}_{n+1}$ defined in the previous section now takes the role of the deformation gradient $\boldsymbol{F}$. The sequence of calculations goes as follows. We assume that the following kinematical variables for particle i at time t_n are given: position $\boldsymbol{x}_{i,n}$, velocity $\boldsymbol{v}_{i,n}$ and acceleration $\boldsymbol{a}_{i,n}$. The update equations consist of semi-implicit sequential calculations of the form [51]

$$\boldsymbol{v}_{i,n+1} = \boldsymbol{v}_{i,n} + \boldsymbol{a}_{i,n}\Delta t \tag{20}$$

$$\boldsymbol{x}_{i,n+1} = \boldsymbol{x}_{i,n} + \boldsymbol{v}_{i,n+1}\Delta t. \tag{21}$$

For stability, the time step is assumed to obey the Courant–Friedrich–Lewy (CFL) condition [29], given by

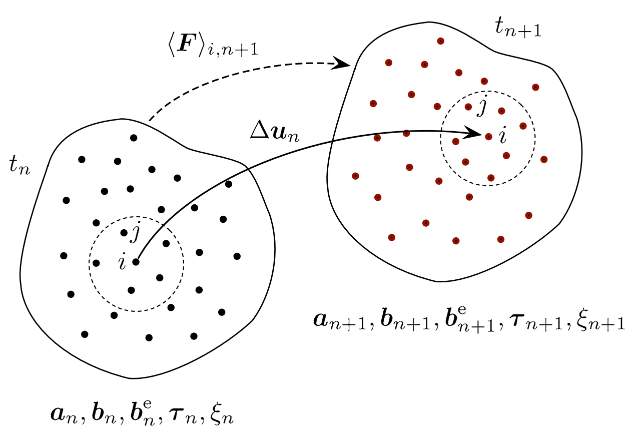

Fig. 1 Configurations of a body at time t_n and time t_{n+1}. The reference configuration is taken at time t_n following the updated Lagrangian approach

$$\Delta t = \alpha \frac{h}{c_v}, \tag{22}$$

where $\alpha < 1$ is a scalar coefficient, h is the smoothing length defined previously, and c_v is the numerical sound speed for the material, usually smaller than the physical sound speed. In all our simulations, we take $\alpha = 0.2$ and

$$c_{v,i} = \sqrt{\frac{E_0}{\rho_{i,0}}}, \tag{23}$$

where E_0 is the initial tangent modulus for the granular material, and $\rho_{i,0}$ is the reference mass density associated with particle i. Furthermore, we take $h = 1.5\Delta$, where Δ is the initial distance between adjacent particles.

The relative deformation gradient with respect to the configuration at time t_n can be calculated as

$$\langle \boldsymbol{F} \rangle_{i,n+1} = \boldsymbol{1} + \sum_{j=1}^{N} \frac{m_j}{\rho_{j,n}} \left(\boldsymbol{u}_{j,n+1} - \boldsymbol{u}_{i,n+1} \right) \otimes \nabla_n W, \tag{24}$$

where W is a kernel function. Note that the gradient of this kernel function is taken with respect to the configuration at time t_n. This deformation gradient produces stresses at time t_{n+1}, which can be evaluated using the update equations from the multiplicative elastoplasticity theory presented in the previous section. The balance of linear momentum (17) can then be used to obtain the acceleration at time t_{n+1}, which, for SPH, takes the form

$$\boldsymbol{a}_{i,n+1} \equiv \left\langle \frac{d\boldsymbol{v}}{dt} \right\rangle_{i,n+1} = \sum_{j=1}^{N} m_j \frac{\left(\boldsymbol{P}_{i,n+1} + \boldsymbol{P}_{j,n+1} \right)}{\rho_{i,n}\rho_{j,n}} \cdot \nabla_n W + \boldsymbol{g}_i, \tag{25}$$

where ρ is mass density, and m_j is mass of particle j. Furthermore, the mass density can be updated through the kinematic relationship

$$\rho_{n+1} = \frac{\rho_n}{J_{n+1}}, \tag{26}$$

where J_{n+1} is the Jacobian of the relative deformation gradient tensor defined in (24).

The kernel chosen for all simulations reported in this paper is the Wendland kernel C6 [18], given in two dimensions by the following expression

$$W(r,h) = \frac{78}{7\pi}(1-r)^8\left(1+8r+25r^2+32r^3\right) \quad 0 \le r \le 1, \tag{27}$$

where $r = \|\boldsymbol{x}_{ij}\|/2h$, and $\boldsymbol{x}_{ij}$ defines the relative position vector of the neighboring particle j with respect to particle i. In this definition of the kernel function, $W = 0$ when $r > 1$. It is worth noting that the gradient of the kernel is taken with respect to the reference coordinates $\boldsymbol{x}_n$, consistent with the updated Lagrangian approach.

Solid boundary conditions require that sediment particles do not penetrate solid boundaries and that some degree of friction between the fluid and boundary is attained. The most widely used method for imposing solid boundary conditions is the dynamic particle (or dummy particle) method. In this method, the solid boundary is modeled with layers of real particles fixed in space or moving with a prescribed motion. These particles enter the equations of motion, in particular, in the calculation of the deformation gradient tensor, generating additional strain on the sediment particles, and hence, changing their stress state as well (through contact). A slightly different approach is proposed in this work to determine the evolution of the strain and stress states of the boundary particles, and it is based on the ideas of Adami et al. [1].

In our approach, the relative displacement between boundary particles and sediment particles is used to evaluate the deformation gradient of the sediment particles only. The stress state of a boundary particle is assigned based only on the stresses of its surrounding sediment neighbors. The stress assigned to a given boundary particle is given by:

$$\boldsymbol{P}_w = \sum_{s=1}^{N_s} \frac{m_s}{\rho_s}\left[\boldsymbol{P}_s + \rho_s \boldsymbol{g} \otimes (\boldsymbol{x}_s - \boldsymbol{x}_w)\right]\tilde{W}_{ws}, \tag{28}$$

where w and s refer to the boundary (wall) and sediment particles, respectively, N_s is the number of sediment neighbors of particle w, and $\tilde{W}_{ws}$ is given by

$$\tilde{W}_{ws} = \frac{W_{ws}}{\sum_{s=1}^{N_s} \frac{m_s}{\rho_s} W_{ws}}. \tag{29}$$

With this approach, the no-slip and no-penetration conditions may be achieved in an approximate sense. The accuracy of the approximation generally depends on the state of motion of the particles in the vicinity of the boundary. If the particles are traveling with considerable speed toward the boundary, for example, then some penetration may still occur. However, in the simulations presented in the next section, we find this technique to be satisfactory for imposing the solid boundary conditions.

4 Comparison with laboratory test results

We have implemented the methodology presented in the previous section into a Python/Cython-based SPH code. The code uses an updated Lagrangian approach in which the reference configuration is updated at every time step, thus avoiding difficulty with very large deformation that typically arises with the total Lagrangian approach [49]. The code structure is fairly simple, with only one main loop that marshals the simulation in time. Within this loop, however, are local iteration loops required by the implicit integration of the multiplicative elastoplasticity theory.

The specific constitutive model we used in the simulations is a hyperelastic-perfectly plastic model with the Drucker–Prager yield criterion. The elastic stored energy function is of the form

$$\Psi = \frac{1}{2}K\ln(J_e)^2 + \mu\|\boldsymbol{e}^{\mathrm{e}}\|^2, \tag{30}$$

where K and μ are the elastic bulk and shear moduli, respectively, J_e is the Jacobian of the elastic deformation gradient tensor, and $\boldsymbol{e}^{\mathrm{e}}$ is the deviatoric part of the logarithmic elastic principal stretches. This elastic constitutive relationship is known as the Henky model [44] and is a finite deformation extension of Hooke's law.

The Drucker–Prager yield criterion is given by

$$\mathcal{F} = \sqrt{3J_2} + \alpha_\phi p - \kappa \le 0, \tag{31}$$

where $J_2 = \|\boldsymbol{s}\|^2/2, \boldsymbol{s}$ is the deviatoric part of $\boldsymbol{\tau}, p = \mathrm{tr}(\boldsymbol{\tau})/3$, and α_ϕ and κ are material parameters related to the Mohr–Coulomb parameters ϕ = internal friction angle and c = cohesion, respectively. For non-associative flow rule, the plastic potential $\mathcal{Q}$ may be written in similar form,

$$\mathcal{Q} = \sqrt{3J_2} + \alpha_\psi p, \tag{32}$$

where α_ψ is a material parameter related to dilation angle ψ. Explicit relationships between ϕ, c, and ψ, and the Drucker–Prager parameters α_ϕ, κ, and α_ψ may be found in [5].

The above constitutive model was used in all of the simulations reported in the following subsections. The laboratory-scale tests simulated include: (a) plane strain collapse tests on dry sand [31]; (b) 3D collapse tests on dry sand [30]; and (c) impact force of dry sand on a rigid wall [34]. For cohesionless material, which is what we assumed in all of the simulations, $c = \kappa = 0$.

4.1 Plane strain collapse of dry sand

In this test, laterally contained dry sand was set free to flow under the action of gravity. Lube et al. [31] determined empirical relationships relating the initial halfwidth d_0 of the sample, and its initial height h_0, to the final runout distance d_∞, and final deposit height h_∞. Figure 2 shows a schematic setup along with the aforementioned dimensions.

In our simulations, we varied the initial column height-to-halfwidth ratio $a = h_0/d_0$ from 0.5 to 10 and selected two values for the internal friction angle, $\phi = 33°$, and $\phi = 37°$, with cohesion c set to zero. These values are about the same as those used in [16, 39, 46] and provide a good basis for comparison of the different solution results. The sand was considered to be in the critical state, and hence, the dilation angle was set to $\psi = 0$. This value of ψ has been supported by many modelers of granular flow behavior, including Peng et al. [38], who used $\psi = 1°$ (i.e., very close to zero), Bui et al. [11], Nonoyama et al. [36], and He and Liang [24], who also reported that the variation of void ratio during the propagation process is relatively small on the basis of experimental observations.

Table 1 summarizes the basic information for each simulation. The initial interparticle distance was set equal to $\Delta = 0.02$ m, the smoothing length to $h = 0.03$ m, and the Young's modulus and Poisson's ratio were set at $E = 20.16$ MPa and $\nu = 0.3$, respectively (which, in turn, determined the elastic bulk and shear moduli, K and μ, respectively, of the Henky model). The time step was taken as $\Delta t = 6 \times 10^{-5}$ s, and the simulation was run for about 1.5 s. We did not apply any artificial viscosity that could reduce stress oscillation, since the latter was quite minor and was not found to be detrimental to the kinematic behavior; see [35].

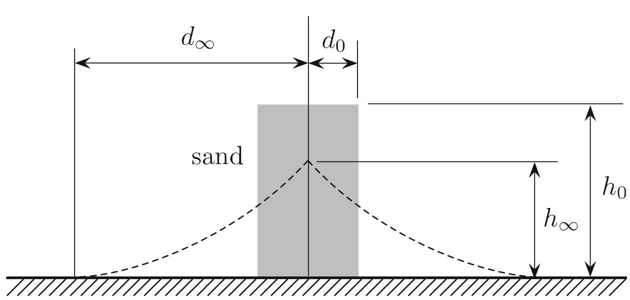

Fig. 2 Two-dimensional plane strain collapse of a rectangular sand body: shaded region denotes initial sand column and dashed curve denotes final configuration

Table 1 Simulations of 2D plane strain collapse tests

Case nos.	h_0 (m)	d_0 (m)	$a = h_0/d_0$	No. of particles	ϕ (deg)
1	0.20	0.40	0.5	1000	33
2	0.20	0.40	0.5	1000	37
3	0.20	0.20	1.0	800	33
4	0.20	0.20	1.0	800	37
5	0.30	0.20	1.5	900	33
6	0.30	0.20	1.5	900	37
7	0.40	0.20	2.0	1000	33
8	0.40	0.20	2.0	1000	37
9	0.80	0.20	4.0	1400	33
10	0.80	0.20	4.0	1400	37
11	1.20	0.20	6.0	2000	33
12	1.20	0.20	6.0	2000	37
13	1.60	0.20	8.0	2400	33
14	1.60	0.20	8.0	2400	37
15	2.00	0.20	10.0	3200	33
16	2.00	0.20	10.0	3200	37

Prior to reporting the results of the simulations, we first conducted sensitivity analyses to determine whether the number of particles used in the simulations was sufficient for the problem at hand. Figure 3 shows three final configurations from the simulations of the plane strain collapse tests with different number of particles. We see that the simulations with medium and high resolutions produced nearly identical final configurations. Thus, we conclude that the results obtained from any of these two simulations would be sufficiently accurate and that there would be no need to go beyond the high-resolution simulation. Snapshots of the configurations at different time instants are shown in Fig. 4 for the simulation with $a = 8.0$ and $\phi = 37°$.

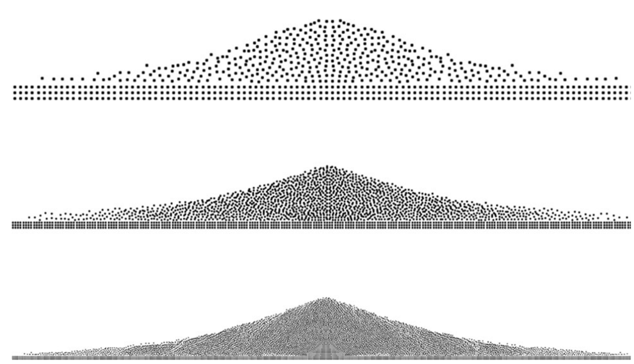

Fig. 3 Final configurations for plane strain sand collapse test with $a = 8.0$ and $\phi = 37°$. Low resolution (top image): 775 particles; medium resolution (middle image): 2400 particles; high resolution (bottom image): 9600 particles

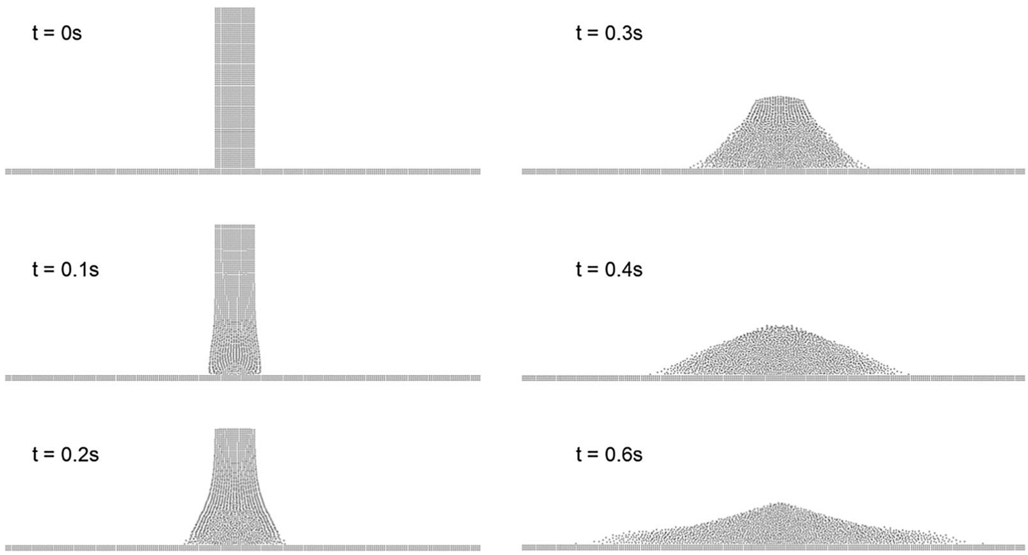

Fig. 4 Snapshots of configurations for simulation of plane strain collapse test with $a = 8.0$ and $\phi = 37°$. Simulation was conducted with 2400 particles

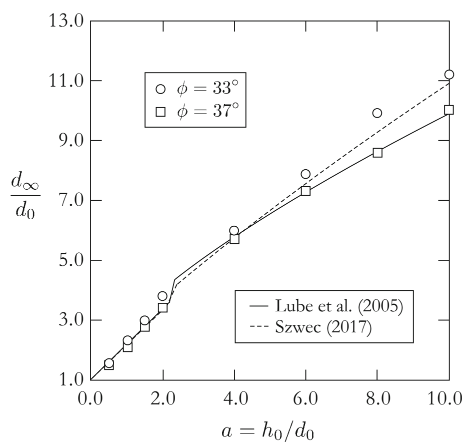

Fig. 5 Two-dimensional plane strain collapse tests on dry sand: non-dimensionalized runout distance versus initial aspect ratio a

Figure 5 presents the results of the simulations in terms of runout distance, determined as the farthest distance from the centerline where the density of particles dropped below around 90–95% of the original density. For comparison purposes, these results are compared with the experimental observations of Lube et al. [31], who concluded that the final geometry of the sand is independent of the internal friction angle of the material and roughness of the boundary. They obtained the following empirical relationships for the final runout distance d_∞ and final height h_∞ as functions of the initial aspect ratio a:

$$\left(\frac{d_\infty}{d_0}\right) = \begin{cases} 1 + 1.2a, & 0 \leq a \leq 2.3, \\ 1 + 1.9a^{2/3}, & a \geq 2.3. \end{cases} \tag{33}$$

$$\left(\frac{h_\infty}{d_0}\right) = \begin{cases} a, & 0 \leq a \leq 1.15, \\ \theta a^{2/5}, & a \geq 1.15. \end{cases} \tag{34}$$

In addition, Lube et al. [31] determined that the coefficient θ appearing in Eq. (34) varies for different tests, with values of $\theta = 1.0$ and $\theta = 1.1$ obtained from the tests.

Referring to Fig. 5, we observe that our formulation is influenced by the internal friction angle, with an intuitive outcome that lower friction angles allow for increased mobility of the sand. The best results were obtained for $\phi = 37°$, and a least squares curve adjusted to our data points yields the following relationship for the runout distance:

$$\left(\frac{d_\infty}{d_0}\right) = \begin{cases} 1 + 1.2a, & 0 \leq a \leq 2.3, \\ 1 + 1.83a^{0.69}, & a \geq 2.3. \end{cases} \tag{35}$$

These results agree well with those reported in [31]. The median error between the curves is around 1.45%, with a standard deviation of 0.71%. Even for the smaller friction angle, our results compare quite well, with the maximum error of approximately 12% for $a > 8.0$.

Figure 6 shows the results for the final height of the deposit along with the empirical relationships presented in [31]. The simulations recover the results from the experimental data very well. In addition, in contrast to the results reported in [31], the calculated final deposit height seems to be less influenced by the internal friction angle ϕ. A least square fit on the simulation data yields the following equation for the final height of the deposit:

$$\left(\frac{h_\infty}{d_0}\right) = \begin{cases} 0.92a, & 0 \leq a \leq 1.15, \\ 1.03a^{2/5}, & a \geq 1.15. \end{cases} \tag{36}$$

Comparing the results for the final height, the error within the linear range is around 8.0%, whereas the error is less than 7.0% in the nonlinear range.

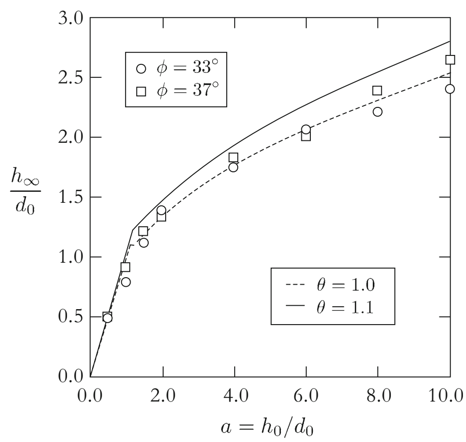

Fig. 6 2D plane strain collapse tests on dry sand: non-dimensionalized final height versus initial aspect ratio a. θ-values from Lube et al. [31]

The discrepancy with the experimental observation that the runout distance is invariant with respect to the internal friction angle needs further elaboration, since the simulations conducted by other authors do not seem to support this observation either, much like our results. Peng et al. [38] used a hypoplastic constitutive model with their SPH code to simulate collapse tests. Their main goal was only to evaluate their hypoplastic implementation, and hence, they conducted only one simulation with $a = 0.5$. They selected a friction angle of $\phi = 33°$ and reported a larger runout distance than the one reported in [31]. This behavior is consistent with our findings. He and Liang [24] also utilized the SPH method along with a viscoplastic constitutive model to simulate dry sand collapse tests. They reported that the conventional Mohr–Coulomb model with a constant friction angle is unable to capture the overall runout dynamics and the final runout distance accurately. They also pointed out that for friction angles less than 33°, the agreement is good only for low values of aspect ratio (i.e., $a < 3$). For higher values of aspect ratio ($a \geq 3$), a value of $\phi = 37°$ yields closer results to the experimental data, while lower values of friction angle overestimate the runout distance. This behavior is also captured by Szewc [46], who simulated collapse tests using $\phi = 31°$ and also observed an overestimation of the runout distance.

4.2 Axisymmetric collapse of dry sand

Lube et al. [30] conducted axisymmetric collapse tests on dry sand. Similar to the plane strain collapse tests, dry sand was initially contained within a cylindrical column resting on a flat surface. The container was then removed instantaneously allowing the sand to flow under gravity. Figure 7 shows the initial and final schematic configurations of the sand.

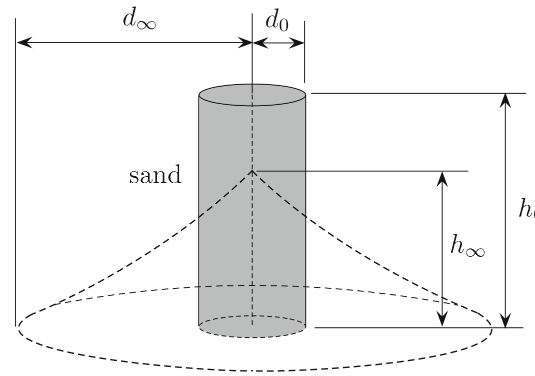

Fig. 7 Axisymmetric collapse of a cylindrical sand body: shaded region denotes initial sand column, dashed curve denotes final configuration

For the axisymmetric experiments, Lube at el. [30] proposed the following equations to estimate the final runout radius and height of the sand column:

$$\left(\frac{d_\infty}{d_0}\right) = \begin{cases} 1 + 1.24a, & 0 \leq a \leq 1.7, \\ 1 + 1.6a^{1/2}, & a \geq 1.7; \end{cases} \tag{37}$$

$$\left(\frac{h_\infty}{d_0}\right) = \begin{cases} a, & 0 \leq a \leq 1.0, \\ 0.88a^{1/6}, & a \geq 1.0, \end{cases} \tag{38}$$

where a is the initial column height-to-radius ratio. Note that Eqs. (37) and (38) differ only slightly from the plane strain empirical relations presented earlier.

The aforementioned axisymmetric collapse tests were simulated as a 3D problem. Before reporting the results of our simulations, however, we first demonstrate that our model can reproduce a well-known result that the final collapsed configuration for a shorter and stouter sand column has a flatter top surface compared to the collapsed configuration for a taller and more slender sand column, which has a more conical shape. This is evident in Figs. 8 and 9 for simulations with $a = 0.5$ and $a = 4.0$, respectively.

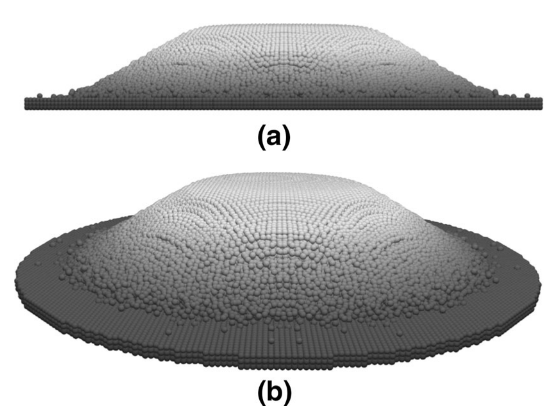

Fig. 8 Final collapsed configuration for a cylindrical sand column with $\phi = 37°$ and $a = 0.5$: **a** elevation and **b** isometric view. Simulation was conducted with 27,000 particles

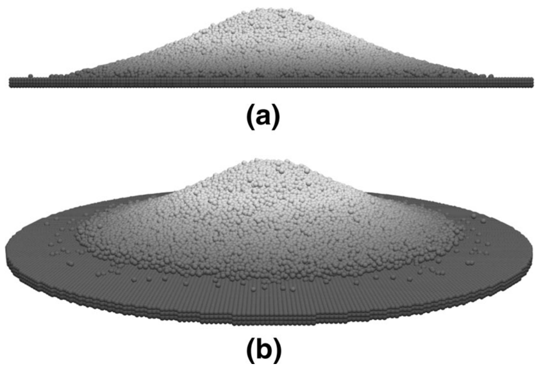

Fig. 9 Final collapsed configuration for a cylindrical sand column with $\phi = 37°$ and $a = 4.0$: **a** elevation and **b** isometric view. Simulation was conducted with 177,000 particles

To obtain solutions that are comparable in accuracy to those obtained from the plane strain simulations, approximately 100 times as many particles were used. Table 2 summarizes the basic information for each simulation. The initial interparticle distance was 0.01, which is about half the distance used for the plane strain simulations, and the smoothing length h was 0.015; Young's modulus and Poisson's ratio were the same as those used for the plane strain simulations. Figures 10 and 11 summarize the results for runout distance and final height, respectively.

From the new set of computer-generated points, we obtain the following least square equations for the final runout distance and column height:

$$\left(\frac{d_\infty}{d_0}\right) = \begin{cases} 1 + 1.11a, & 0 \le a \le 1.7, \\ 1 + 1.66a^{0.48}, & a \ge 1.7. \end{cases} \tag{39}$$

$$\left(\frac{h_\infty}{d_0}\right) = \begin{cases} 0.87a, & 0 \le a \le 1.0, \\ 0.87a^{0.16}, & a \ge 1.0. \end{cases} \tag{40}$$

For the runout equation, the median error for the nonlinear part is less than 1.3%, with a standard deviation of 0.73%. For the linear part, the error is 10.5%. In terms of final height, the error in our equation is 13% for the linear part of the curve, while for the nonlinear part, the median error is 5.25% with standard deviation of 1.62% within the range $2 \le a \le 4$. If we extrapolate our adjusted curve for larger values of a, the expected error is less than 18%.

Table 2 Simulations of axisymmetric collapse tests modeled as 3D problems

Case nos.	h_0 (m)	d_0 (m)	$a = h_0/d_0$	No. of particles	ϕ (deg)
1	0.10	0.20	0.5	27,712	33
2	0.10	0.20	0.5	27,712	37
3	0.20	0.20	1.0	44,338	33
4	0.20	0.20	1.0	44,388	37
5	0.40	0.20	2.0	88,678	33
6	0.40	0.20	2.0	88,678	37
7	0.80	0.20	4.0	177,484	33
8	0.80	0.20	4.0	177,484	37

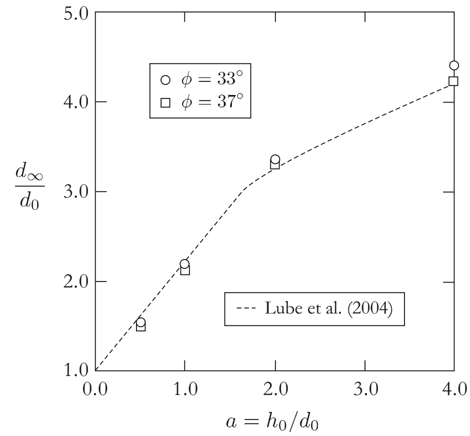

Fig. 10 Three-dimensional axisymmetric collapse tests on dry sand: non-dimensionalized runout distance versus initial aspect ratio a

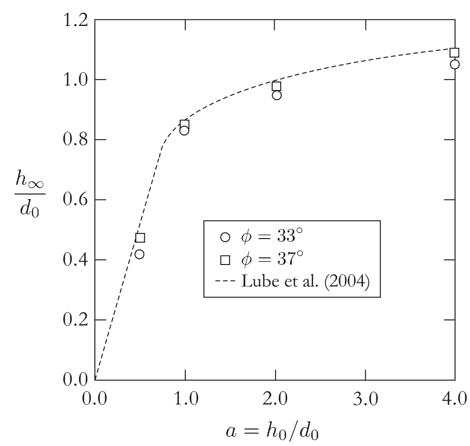

Fig. 11 Three-dimensional axisymmetric collapse tests on dry sand: non-dimensionalized final height versus initial aspect ratio a

4.3 Impact force of sand on a rigid wall

Moriguchi et al. [34] conducted a series of laboratory experiments on dry Toyoura fine sand released on an inclined flume to impact a rigid wall at the base of the flume. The objective of the experiment was to obtain detailed information on the magnitude of the impact force as a function of the flume inclination, as well as to test their granular flow model employing CFD calculations based on an Eulerian formulation. The sand was nearly uniform with grain sizes $D_{10} = 0.206$ mm, $D_{30} = 0.241$ mm, $D_{50} = 0.273$ mm, and $D_{60} = 0.281$ mm, where the subscripts denote percent finer; minimum and maximum grain sizes were 0.102 and 0.425 mm, respectively. Specific gravity of the solid phase was measured as 2.65, and density tests showed minimum and maximum void ratios of 0.61 and 0.97, respectively.

The sand was initially contained in a box atop the flume and then was suddenly released through a side door to impact a rigid wall waiting at the bottom of the flume. A force transducer attached to the wall recorded the impact force as a function of time for different flume inclinations, which varied from 45° to 65°. Moriguchi et al. [34] noted that the timing of sand release was not synchronized with that of the sensor, and thus, for flume inclination of 45°, for example, they had to rely on a video camera to infer the arrival time of the sand. However, this did not affect the shape of the impact force–time curve. Figure 12 shows the initial setup for flume inclination of 45°, which is the configuration simulated in the present study. Table 3 summarizes the parameters used in the simulations.

Figure 13 shows snapshots of the sand configurations at different time instants for flume inclination of 45°. In generating these configurations, the experiments were modeled as a plane strain problem with 1500 sand particles and 1317 boundary particles. The figure suggests that after contact with the wall, the particles stopped moving almost immediately, and a static wedge forms between the flow and the wall. This wedge grows in size and at some point reaches the top of the wall barrier. This behavior is consistent with the experimental observations and numerical results of [40]. In our simulation, some spillage over the wall occurs, as can be seen in the last four frames of Fig. 13. It is interesting to note that the simulation for $\phi = 35°$ predicted an angle of repose of approximately 35°, as seen from the frame corresponding to $t = 3.0$ s.

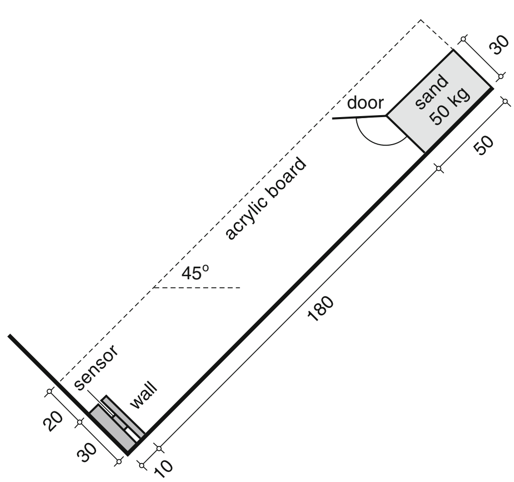

Fig. 12 Inclined flume and sand box configuration for granular flow experiment. Dimensions are in cm. After Moriguchi et al. [34]

Table 3 Simulation of impact force of granular flow on a rigid wall

Parameter	Value
Mass m	0.138 kg
Density ρ	1379 kg/m^3
Friction angle ϕ	Varies
Dilation angle ψ	0
Spacing Δ	0.01 m
Smoothing length h	0.015 m
Modulus E_0	21.6 MPa
Poisson's ratio ν	0.3
Coefficient c_v	125 m/s
Step size Δt	3×10^{-5} s
Total duration t	3.00 s
Number of steps	100,000

More important than the kinematics of the flow in this case is the ability of our formulation to predict the impact forces. Our proposed boundary formulation is very useful for this purpose since for each time step, we calculate the average stress on the sand using the kernel and extrapolate it to the boundary. To calculate the resultant force, we employ a direct summation of forces on each boundary particle. The resultant force R_n is calculated as follows:

$$R_n = \sum_{b=1}^{N_b} \boldsymbol{P}_b : (\boldsymbol{n}_b \otimes \boldsymbol{n}_b) B\Delta, \tag{41}$$

where $\boldsymbol{n}_b$ is the normal vector to the impacted wall, $B = 0.3$ m is the width of the flume used in the experiments, and N_b is the number of particles at the wall in direct contact with the sand.

Figure 14 shows the calculated impact forces for $\phi = 33°, 35°$, and 44°, along with the experimental measurements and numerical simulation results reported by Moriguchi et al. [34]. A number of observations can be made from these results. First, the values of ϕ within the range of engineering interest seem to have little effect on the predicted maximum impact force. In contrast, the results presented by Moriguchi et al. [34] using their CFD model showed a significant drop in the calculated impact force for $\phi = 40°$. This has important implications, given that we are solving a problem in dynamics where the value of the friction angle has inherent uncertainties. It suggests that our model is predictive because the results do not depend significantly on the uncertainties in the value of ϕ, provided that it lies within the range of engineering interest. Second, we observed some spillage over the top of the wall barrier in all of the simulations, even for $\phi = 44°$ (not shown), whereas Moriguchi et al. [34] noted that spillage was observed only for the simulations with $\phi = 30°$ and

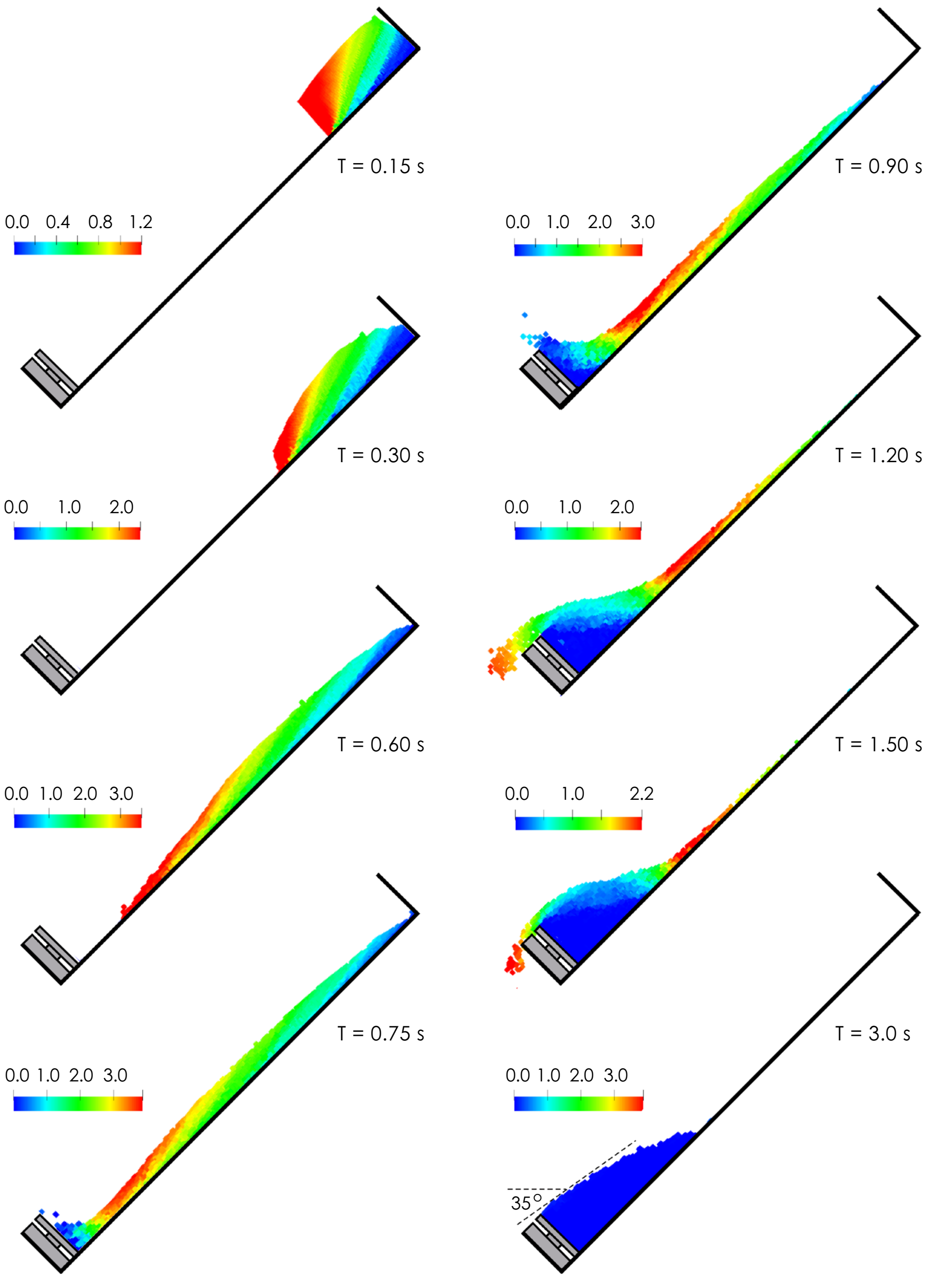

Fig. 13 Snapshots of simulated granular flow down a 45° inclined flume at internal friction angle of 35°. For reference, the 35° angle of repose is indicated at time $t = 3.0$ s. Color bar (electronic version only) is resultant velocity in m/s

35°, but not for $\phi = 40°$ where all of the sand simply stopped in front of the wall, a behavior that we have also observed when we increased ϕ to an unreasonably high value of 60°. Once again, the uncertainties in the value of ϕ do not seem to influence the resulting kinematics significantly. Finally, all of the calculated peak impact forces, including the ones reported by Moriguchi et al. [34] for $\phi = 30°$ and 35°, overestimated the measured response by around 15%. For our own simulations, this could be due to the fact that we did not introduce any viscosity into the model, which could have slowed down the flow and reduced the impact force. As an aside, the effect of viscosity can easily be accommodated in our formulation through an extension of the multiplicative plasticity theory to viscoplasticity [42].

Finally, Fig. 15 compares the calculated impact forces for two analyses with different number of particles, suggesting that the numerical results are sufficiently accurate.

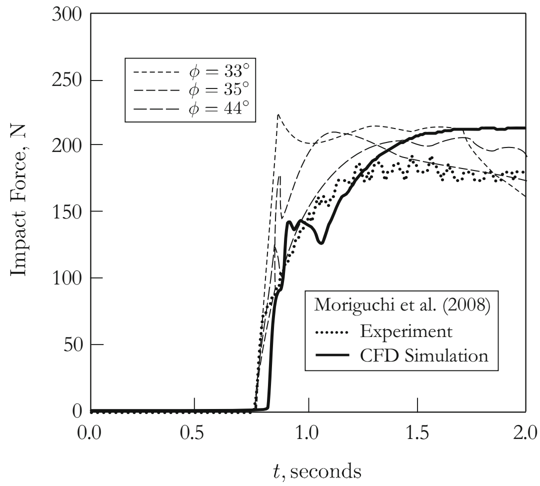

Fig. 14 Impact force versus time for flume inclination of 45°. Simulation of Moriguchi et al. [34] assumed that $\phi = 35°$. Results from SPH simulations suggest that, within the range of engineering interest, the internal friction angle ϕ has little effect on the calculated maximum impact force

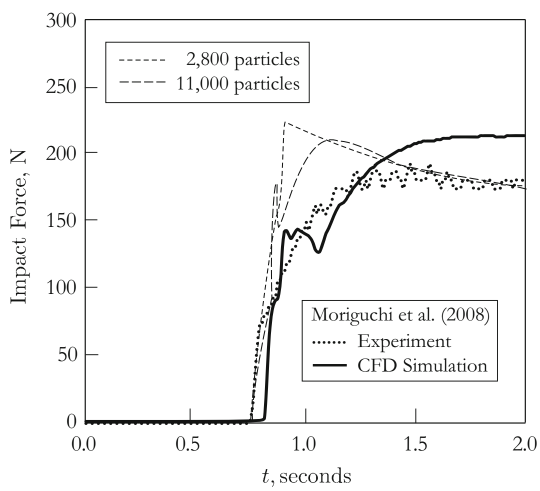

Fig. 15 Impact force versus time for flume inclination of 45°: Assuming a friction angle of 35°, increasing the number of particles four times changes the calculated maximum impact force by less than 5%

To summarize, the above results demonstrate the predictive capability of our model for laboratory-scale experiments, as well as suggest its potential applications for field-scale problems.

5 Conclusions

We have presented an updated Lagrangian finite deformation version of the SPH method employing a multiplicative decomposition of the deformation gradient. To the knowledge of the authors, this is the first time that such formulation has been applied for granular flows in the context of the SPH method. There are numerous advantages of such formulation, including the facts that: (a) One does not have to deal with the issue of what objective stress rate to use, which is an unresolved issue in the hypoelastic framework; (b) the effects of the so-called tensile instability can be reduced with the updated Lagrangian approach, or even eliminated with the total Lagrangian approach [50]; and (c) the computational costs can be reduced significantly when the neighbor search procedure is only performed every certain number of steps, and not every step as done in the conventional SPH procedure. A boundary condition formulation adopted from the work of [1] and cast into the finite deformation framework has also been implemented. This formulation is simple and straightforward to incorporate into any SPH code. In all of our tests, we have been able to impose the no-penetration condition, as well as successfully attained the no-slip condition.

The new framework has been used to simulate laboratory-scale experiments with dry sand. We have been able to reproduce the experimental data both qualitatively and quantitatively. Furthermore, results of our simulations generally agree with those reported by other modelers. One notable result from the impact force simulations is that the predicted impact force and the calculated flow kinematics do not seem to be strongly affected by the value of the internal friction angle. Given that the value of the internal friction angle determined from quasi-static tests cannot be readily extrapolated to dynamic granular flow problems, this observation indicates that our model is predictive for laboratory-scale applications and has the potential for application to similar field-scale problems.

Acknowledgements The first author acknowledges the financial support of the National Council for Scientific and Technological Development in Brazil. Additional funding was provided by the John A. Blume Earthquake Engineering Center at Stanford University. This work was supported in part by the U.S. National Science Foundation under Award Number CMMI-1462231.

References

1. Adami S, Hu XY, Adams NA (2012) A generalized wall boundary condition for smoothed particle hydrodynamics. J Comput Phys 231:7057–7075
2. Bandara S, Ferrari A, Laloui L (2016) Modelling landslides in unsaturated slopes subjected to rainfall infiltration using material point method. Int J Numer Anal Methods Geomech 40(9):1358–1380
3. Becker PA, Idelsohn SR (2016) A multiresolution strategy for solving landslides using the particle finite element method. Acta Geotech 11:643–657
4. Bonet J, Lok TSL (1999) Variational and momentum preservation aspects of smooth particle hydrodynamic formulations. Comput Methods Appl Mech Eng 180:97–115

5. Borja RI (2013) Plasticity modeling & computation. Springer, Berlin
6. Borja RI, White JA (2010) Continuum deformation and stability analyses of a steep hillside slope under rainfall infiltration. Acta Geotech 5(1):1–14
7. Borja RI, Liu X, White JA (2012) Multiphysics hillslope processes triggering landslides. Acta Geotech 7(4):261–269
8. Borja RI, White JA, Liu X, Wu W (2012) Factor of safety in a partially saturated slope inferred from hydro-mechanical continuum modeling. Int J Numer Anal Methods Geomech 38(2):236–248
9. Bui HH, Fukugawa R (2013) An improved SPH method for saturated soils and its application to investigate the mechanisms of embankment failure: case of hydrostatic pore-water pressure. Int J Numer Anal Methods Geomech 37:31–50
10. Bui HH, Sako K, Fukugawa R (2007) Numerical simulation of soil-water interaction using smoothed particle hydrodynamics (SPH) method. J Terrramech 44:339–346
11. Bui HH, Fukugawa R, Sako K, Ohno S (2008) Lagrangian meshfree particles method (SPH) for large deformation and failure flows of geomaterial using elastic–plastic soil constitutive model. Int J Numer Anal Methods Geomech 32:1537–1570
12. Bui HH, Fukugawa R, Sako K, Wells C (2011) Slope stability analysis and discontinuous slope failure simulation by elasto-plastic smoothed particle hydrodynamics (SPH). Géotechnique 361(7):565–574
13. Calvetti F, di Prisco CG, Vairaktaris E (2017) DEM assessment of impact forces of dry granular masses on rigid barriers. Acta Geotech 12:129–144
14. Camargo J, Quadros Velloso R, Vargas EA Jr (2016) Numerical limit analysis of three-dimensional slope stability problems in catchment areas. Acta Geotech 11(6):1369–1383
15. Cen D, Huang D, Ren F (2017) Shear deformation and strength of the interphase between the soilrock mixture and the benched bedrock slope surface. Acta Geotech 12:391–413
16. Chen W, Qiu T (2011) Numerical simulations of granular materials using smoothed particle hydrodynamics method. Geotech Spec Publ ASCE 217:157–164
17. Chen JS, Pan C, Wu CT, Liu WK (1996) Reproducing kernel particle methods for large deformation analysis of non-linear structures. Comput Methods Appl Mech Eng 139(1–4):195–227
18. Dehnen W, Aly H (2012) Improving convergence in smoothed particle hydrodynamics simulations without pairing instability. Mon Not R Astron Soc 425:1068–1082
19. Fern EJ, Soga K (2015) The role of constitutive models in MPM simulations of granular column collapses. Acta Geotech 11(3):659–678
20. Gholami Khorzani M, Galindo-Torres SA, Scheuermann A, Williams DJ (2017) SPH approach for simulating hydro-mechanical processes with large deformations and variable permeabilities. Acta Geotech. https://doi.org/10.1007/s11440-017-0610-9
21. Gingold RA, Monaghan JJ (1977) Smoothed particle hydrodynamics: theory and application to non-spherical stars. Mon Not R Astron Soc 181:375–389
22. Gray JP, Monaghan JJ, Swift RP (2001) SPH elastic dynamics. Comput Methods Appl Mech Eng 190:6641–6662
23. Guo X, Peng C, Wu W, Wang Y (2016) A hypoplastic constitutive model for debris materials. Acta Geotech 11:1217–1229
24. He X, Liang D (2015) Study of the runout of granular columns with SPH methods. Int J Offshore Polar Eng 25(4):281–287
25. Kakogiannou E, Sanavia L, Nicot F, Darve F, Schrefler BA (2016) A porous media finite element approach for soil instability including the second-order work criterion. Acta Geotech 11(4):805–825
26. Lai X, Ren B, Fan H, Li S, Wu CT, Regueiro RA, Liu L (2015) Peridynamics simulations of geomaterial fragmentation by impulse loads. Int J Numer Anal Methods Geomech 39(12):1304–1330
27. Lee EH (1969) Elastic–plastic deformation at finite strains. J Appl Mech 36:1–6
28. Lei X, Yang Z, He S, Liu E, Wong H, Li X (2017) Numerical investigation of rainfall-induced fines migration and its influences on slope stability. Acta Geotech 12(6):1431–1446
29. Liu GR, Liu MB (2003) Smoothed particle hydrodynamics: a meshfree particle methods. World Scientific, Singapore
30. Lube G, Huppert HE, Stephen R, Sparks J, Hallworth MA (2004) Axisymmetric collapses of granular columns. J Fluid Mech 508:175–199
31. Lube G, Huppert HE, Stephen R, Sparks J, Freundt A (2005) Collapses of two-dimensional granular columns. Phys Rev E 72(4):041301
32. Lucy LB (1977) A numerical approach to the testing of the fission hypothesis. Astron J 82(12):1013–1024
33. Meng X, Wang Y, Wang C, Fischer J-T (2017) Modeling of unsaturated granular flows by a two-layer approach. Acta Geotech 12(3):677–701
34. Moriguchi S, Borja RI, Yashima A, Sawada K (2009) Estimating the impact force generated by granular flow on a rigid obstruction. Acta Geotech 4:57–71
35. Nguyen CT, Nguyen CT, Bui HH, Nguyen GD, Fukugawa R (2017) A new SPH-based approach to simulation of granular flows using viscous damping and stress regularisation. Landslides 14(1):69–81
36. Nonoyama H, Moriguchi S, Sawada K, Yashima A (2015) Slope stability analysis using smoothed particle hydrodynamics (SPH) method. Soils Found 55(2):458–470
37. Pastor M, Yague A, Stickle MM, Manzanal D, Mira P (2018) A two-phase SPH model for debris flow propagation. Int J Numer Anal Methods Geomech 42(3):418–448
38. Peng C, Wu W, Yu HS, Wang C (2015) A SPH approach for large deformation analysis with hypoplastic constitutive model. Acta Geotech 10:703–717
39. Peng C, Guo X, Wu W, Wang Y (2016) Unified modelling of granular media with smoothed particle hydrodynamics. Acta Geotech 11:1231–1247
40. Pudasaini SP, Hutter K, Hsiau SS, Tai SC, Wang Y, Katzenbach R (2007) Rapid flow of dry granular materials down inclined chutes impinging on rigid walls. Phys Fluids 19:053302
41. Simo JC (1992) Algorithms for static and dynamic multiplicative plasticity that preserve the classical return mapping schemes of the infinitesimal theory. Comput Methods Appl Mech Eng 99:61–112
42. Simo JC, Hughes TJR (1998) Computational inelasticity. Springer, New York
43. Siriaksorn T, Chi S-W, Foster C, Mahdavi A (2018) *u–p* semi-Lagrangian reproducing kernel formulation for landslide modeling. Int J Numer Anal Methods Geomech 42(2):231–255
44. Souza Neto E, Peric D, Owens D (2008) Computational methods for plasticity: theory and applications. Wiley, London
45. Sulsky D, Chen Z, Schreyer HL (1994) A particle method for history-dependent materials. Comput Methods Appl Mech Eng 118(1–2):179–196
46. Szewc K (2017) Smoothed particle hydrodynamics modeling of granular column collapse. Granul Matter 19:3
47. Teufelsbauer H, Wang y, Pudasaini SP, Borja RI, Wu W (2011) DEM simulation of impact force exerted by granular flow on rigid structures. Acta Geotech 6:119–133
48. USGS (2018) USGS Geologists join efforts in Montecito to assess debris-flow aftermath. https://www.usgs.gov/news/usgs-

geologists-join-efforts-montecito-assess-debris-flow-aftermath. Accessed 2 Mar 2018
49. Vidal Y, Bonet J, Huerta A (2007) Stabilized updated Lagrangian corrected SPH for explicit dynamic problems. Int J Numer Methods Eng 69:2687–2710
50. Vignjevic R, Reveles JR, Campbell J (2006) SPH in a total Lagrangian formalism. Comput Model Eng Sci 14(3):181–198
51. Violeau D (2012) Fluid mechanics and the SPH method: theory and applications. Oxford University Press, Oxford
52. Zhang W, Maeda K, Saito H, Li Z, Huang Y (2016) Numerical analysis on seepage failures of dike due to water level-up and rainfall using a water–soil-coupled smoothed particle hydrodynamics model. Acta Geotech 11:1401–1418